DENTAL MATERIALS XXX (2020) XXX–XXX

Available online at www.sciencedirect.com

ScienceDirect

journal homepage: www.intl.elsevierhealth.com/journals/dema

Mechanophysical and biological properties of a 3D-printed titanium alloy for dental applications

Jae-Heon Kim[a,b,c,1], *Moon-Young Kim*[b,d,1], *Jonathan C. Knowles*[c,e,f,g], *Sunyoung Choi*[h], *Hyejong Kang*[i], *Sang-hyun Park*[j], *Sung-Min Park*[b,c], *Hae-Won Kim*[a,b,c], *Jong-Tae Park*[k,*], *Jung-Hwan Lee*[a,b,c,**], *Hae-Hyoung Lee*[a,b,***]

[a] *Department of Biomaterials Science, College of Dentistry, Dankook University, 119 Dandae-ro, Cheonan, Chungcheongnam-do 31116, Republic of Korea*

[b] *Institute of Tissue Regeneration Engineering (ITREN), Dankook University, 119 Dandae-ro, Cheonan, Chungcheongnam-do 31116, Republic of Korea*

[c] *Department of Nanobiomedical Science & BK21 PLUS NBM Global Research Center for Regenerative Medicine Research Center, Dankook University, 119 Dandae-ro, Cheonan, Chungcheongnam-do 31116, Republic of Korea*

[d] *Department of oral and maxillofacial surgery, College of Dentistry, Dankook University, 119 Dandae-ro, Cheonan, Chungcheongnam-do 31116, Republic of Korea*

[e] *UCL Eastman-Korea Dental Medicine Innovation Centre, Dankook University, 119 Dandae-ro, Cheonan, Chungcheongnam-do 31116, Republic of Korea*

[f] *Division of Biomaterials and Tissue Engineering, Eastman Dental Institute, University College London, London, UK*

[g] *The Discoveries Centre for Regenerative and Precision Medicine, Eastman Dental Institute, University College London, London, UK*

[h] *Department of Prosthodontics, Sejong Dental Hospital, School of Dentistry, Dankook University, Sejong, Chungcheongnam-do, 30107, Republic of Korea*

[i] *Department of Orthodontics, Sejong Dental Hospital, School of Dentistry, Dankook University, Sejong, Chungcheongnam-do 30107, Republic of Korea*

[j] *Osong Research Institute, TaeWoong Medical Co., Ltd, 55-7, Osongsaengmyeong 2-ro, Republic of Korea*

[k] *Department of Oral Anatomy, College of Dentistry, Dankook University, 119 Dandae-ro, Cheonan, Chungcheongnam-do 31116, Republic of Korea*

ARTICLE INFO

Article history:
Received 12 March 2020
Received in revised form
20 April 2020
Accepted 30 April 2020
Available online xxx

ABSTRACT

Objective. Titanium and its alloys are widely used for dental and medical biomaterials due to their excellent mechanical and biological advantages. After the introduction of direct laser metal sintering (DLMS) 3D printing technology and its use over conventional machine-cut processes, questions remain regarding whether 3D-printed titanium (alloy) devices have similar biological properties to machine-cut counterparts for dental applications. Thus, this work focuses on comparing the biological activities of machine-cut and 3D-printed

* *Corresponding author*. Department of Oral Anatomy, College of Dentistry, Dankook University, 119 Dandae-ro, Cheonan, Chungcheongnam-do 31116, Republic of Korea.

** *Corresponding author at*: Institute of Tissue Regeneration Engineering (ITREN), Dankook University, 119 Dandae-ro, Cheonan, Chungcheongnam-do 31116, Republic of Korea.

*** *Corresponding author at*: Department of Biomaterials Science, College of Dentistry, Dankook University, 119 Dandae-ro, Cheonan, Chungcheongnam-do 31116, Republic of Korea.

E-mail addresses: wogjs199@naver.com (J.-H. Kim), kmyomfs@dankook.ac.kr (M.-Y. Kim), j.knowles@ucl.ac.uk (J.C. Knowles), annejane@hanmail.net (S. Choi), hyejongk@dankook.ac.kr (H. Kang), shpark1@stent.net (S.-h. Park), hahatype12@naver.com (S.-M. Park), kimhw@dku.edu (H.-W. Kim), jongta2@dankook.ac.kr (J.-T. Park), ducious@gmail.com (J.-H. Lee), haelee@dku.edu (H.-H. Lee).

[1] These authors contributed equally to this work as first authors.

https://doi.org/10.1016/j.dental.2020.04.027

Please cite this article in press as: Kim J-H, et al. Mechanophysical and biological properties of a 3D-printed titanium alloy for dental applications. Dent Mater (2020), https://doi.org/10.1016/j.dental.2020.04.027

Keywords:
3D printing
Dental application
Titanium alloy
Osteogenesis

specimens after optimizing the DLMS 3D-printing conditions in terms of the mechanophysical characteristics.

Methods. The DLMS 3D-printing (as a function of the laser spacing from 30–100 μm) and post-surface treatment (as-given or sand-blasted) conditions were optimized using medical-grade Ti-6Al-4V powders in terms of the inner pore amount, mechanical properties, roughness and hydrophilicity. Then, the initial cell adhesion of the optimized DLMS 3D-printed Ti-6Al-4V specimen was compared with that of the machine-cut Ti-6Al-4V specimen against human dermal fibroblasts (hDFs) and mesenchymal stem cells (hMSCs), which are representative of direct-contact cell types of orofacial mucosa and bone, respectively. hMSC differentiation on the specimens was conducted for up to 21 days to measure the osteogenic gene expression and biomineralization.

Results. Laser spacings of 30–40 μm had fewer inner defects and consequently a higher three-point flexural strength and elastic modulus compared to other larger laser spacings. Depending on the span width (0.3–1 mm) in the lattice architecture, the elastic modulus of the 3D-printed cuboid specimen can be further controlled (up to ~30 times). The sand-blasted specimens after 3D printing revealed lower surface roughness and higher hydrophilicity compared to the as-3D printed specimen, which were considered optimal conditions for biological study. Initial hDF and hMSC adhesion for 12 hr and hMSC differentiation on the surface were comparable between the sand-blasted 3D-printed and machine-cut specimens in terms of adherent cell numbers, vinculin intensity, osteogenic gene expression and biomineralization.

Significance. The optimized DLMS 3D-printed Ti-6Al-4V specimen had similar biological properties to those of the machine-cut counterpart, suggesting the potential usefulness of 3D printing technology for a wide range of dental applications.

1. Introduction

Biomaterials used in dental and medical areas must demonstrate appropraite mechanophysical and biological properties to achieve a high degree of biofunctionality [1–5]. Titanium and its alloys are widely used for dental and orthopedic applications due to their low density, excellent mechanical properties and great biocompatibility [6]. Until now, titanium and its alloys have generally been produced for medical use by machining titanium rods or plates by computer numerical control (CNC) machines and subjecting them to various surface modifications to improve the mechanical properties and biological response [7]. Thus, machine-cut titanium and its alloys with appropriate surface modifications have become widely-used biomaterials in clinical settings [8].

Within the last 15 years, direct laser metal sintering (DLMS) as a 3D printing technology was introduced as a promising fabrication technology for titanium and its alloys [9–15]. Then, it became commercially available due to its great reproducibility, good customizing ability for obtaining complex architectures with controllable surface geometry, cost effectiveness for the fabrication of individual parts and relatively good resolution (~20 μm), which attracted a myriad of dental applications, such as implantable devices (i.e. dental implants and scaffolds) and prosthetic devices (i.e. dental crowns and denture frameworks) [16–18].

The main merits of utilizing DLMS 3D-printed titanium (alloy)-based medical devices are the excellent mechanical properties due to the low density and versatility of the architectures obtainable to mimic the natural anatomical 3D geometries of hard tissues [19]. For even accelerating osteogenesis, the micro or macro porosity, surface roughness, and drug loading capacity can be further optimized to accelerate biological response, while maintaining the mechanical properties [20–22]. However, questions remain regarding whether optimized 3D-printed medical devices have similar biological capacities to machine-cut counterparts, especially for dental applications [20,21].

Therefore, the aim of this study is to compare the biological activities of machine-cut and 3D-printed specimens after optimizing the 3D-printing conditions. To achieve this target, DLMS 3D-printing (as a function of the laser spacing from 30 to 100 μm) and post-surface treatment (as-given or sand-blasted) conditions were optimized using medical-grade Ti-6Al-4V powders (grade 5) in terms of the mechanophysical properties, such as the inner defect levels, mechanical properties, roughness and hydrophilicity. Then, the biological effects of optimized DLMS 3D-printed Ti-6Al-4V specimens were compared with those of machine-cut Ti-6Al-4V specimens against human dermal fibroblasts (hDFs) and mesenchymal stem cells (hMSCs), which are representative direct-contact cell types of orofacial mucosa and bone, respectively. Thus, the first null hypothesis of this study is that there are no differences in the mechanical properties relative to the laser spacing (30–100 μm). The second null hypothesis is that there are no differences in the biological activities, such as the cell adhesion and osteogenic capacity of stem cells, between the optimized 3D-printed and machine-cut specimens.

Please cite this article in press as: Kim J-H, et al. Mechanophysical and biological properties of a 3D-printed titanium alloy for dental applications. Dent Mater (2020), https://doi.org/10.1016/j.dental.2020.04.027

Table 1 – Summary of the experimental groups and specimen types.

Method	Manufacturing process	Experimental parameter	Detail conditions	Specimen types
Fe-SEM analysis for pore detection	3D-printing	Laser gap	30, 40, 50, 60, 70, 80, 90, or 100 μm	Disk (d = 10 mm and h = 2 mm)
Flexural strength and fractography	3D-printing	Laser gap	30, 50, 70, or 90 μm	Bar specimens (25.0 x 4.0 x 2.0 mm)
Modulus from lattice architecture	3D-printing (50 μm laser gap)	Lattice span width	0.3, 0.5, or 1 mm	Lattice structures (10.0 x 10.0 x 20.0 mm)
Surface analysis	3D-printing (50 μm laser gap)	Post-surface treatment after 3D-printing	As printed, sand-blasting, or polishing	Disk (d = 10 mm and h = 2 mm)
In vitro analysis	3D-printing (50 μm laser gap) or machined-cut	Manufacturing method	3D-printing or machined-cut	Disk (d = 10 mm and h = 2 mm)

2. Materials and methods

2.1. *Specimen preparation*

All specimens used in this study except for the as-provided machined-cut specimens used for the biological assay control group were prepared by selective laser melting 3D printing technology. The particle size of the Ti-6Al-4V powder (grade5, Advanced Powders & Coatings Inc. QC, Canada) was measured by a particle size analyser (LA-950V2, HORIBA, Kyoto, Japan), and the images and compositions of the powder were obtained by field emission scanning electron microscopy (FE-SEM, Sigma 300, ZEISS, Oberkochen, Germany) on an instrument equipped with energy-dispersive spectroscopy (EDS) (Oxford). The specimens were fabricated in an argon atmosphere, in accordance with the output conditions (radiation power of 225 W and scanning rate of 1200 mm/s) using a DLMS 3D printer (SM250, Sentrol Co., Ltd, Seoul, Korea) with a Yb (Ytterbium) fiber laser wavelength of 1060 nm. To optimize the 3D printing conditions, the disk specimens (10 mm diameter and 2 mm thickness) were fabricated according to the different laser spacings (30, 40, 50, 60, 70, 80, 90, or 100 μm). The minimum value for the laser gap was set at 30 μm based on average diameter of Ti6Al4 V powder (~37.5 μm) where the laser gap for DLMS should be similar or larger than the powder diameter to sinter two individual powders together for 3D-printing. All of the specimens, except the lattice structure, were 3D-printed with a 45-degree axis. To test the mechanical properties, bar specimens (25.0 × 4.0 × 2.0 mm) and lattice structures (10.0 × 10.0 × 20.0 mm) with different span widths (0.3, 0.5, 1 mm or block type) were prepared. The single lattice sizes were 3, 4, and 5 mm for the 0.3, 0.5, and 1 mm span width groups, respectively. The bar specimens were made from different laser spacings (30, 50, 70, and 90 μm) for the three-point flexural strength test, and the lattice structures were made with a 50 μm laser spacing. The edges of the bar specimens were chamfered with P600 SiC paper and sand-blasted with 50 μm alumina at 4.3 bar pressure using a sandblaster (Basic Classic, Renfert, Hilzingen, Germany) for 60 s to clean the whole surfaces. Lattice structures with different gaps were made for varying the elastic modulus of the Ti-6Al-4V construction. For the surface characterization and cell experiments, disk specimens (with a 10 mm diameter and 2 mm thickness) were made with a 50 μm laser spacing. The disk specimens were divided into 3 subgroups: 'as 3D-printed', '3D + polished', and '3D + sand-blasted'. The as 3D-printed group was not surface-treated after 3D printing. The 3D + sand-blasted group was sand-blasted on one surface for 60 seconds with 50 μm alumina at 4.3 bar pressure using the aforementioned sandblaster. The 3D + polished group was polished with P220-SiC paper to obtain a flat surface. The completed specimens were serially cleaned for 5 min each in acetone, ethanol and distilled water in an ultrasonic chamber (Table 1).

2.2. *Surface pores and total pore area in cross-sectioned specimen*

The disk specimens (with a 10 mm diameter and 2 mm thickness) with different laser spacings (30, 40, 50, 60, 70, 80, 90, and 100 μm) were vertically embedded in epoxy resin (EpoFix Kit, Struthers, Ballerup, Denmark) for visualizing the cross-sectional plane to detect surface pores and total pore area. The specimens were serially polished using a polisher (LaboPol-5, Strouers, Ballerup, Denmark) with P220 ~ 4000-grit SiC papers. After the specimens were cleaned with distilled water and coated with Pt, scanning electron microscopy (SEM, JSM-6510, JEOL Ltd., Tokyo, Japan) images were captured. The surface pore numbers and total pore area were measured by using an image measurement program (ImageJ version 1.46, USA) at 3 sites per specimen and then averaged ($n = 3$) [23]. The minimum value of the pore area was set at 0.4 mm^2.

2.3. *Mechanical properties and fractography*

The flexural strength of the bar specimens (25.0 × 4.0 × 2.0 mm) with different laser spacings (30, 50, 70, and 90 μm) was measured by the three-point flexural strength test at a 20 mm span length ($n = 5$) using a universal testing machine (Instron 5966, Instron, MA, USA) at a crosshead speed of 1 mm/min. The three-point flexural strength (σ, N/mm^{-2}), was calculated by the following formula ($\sigma = 3PL/2wt^2$), where P is the maximum flexure load (N), L is the length of the support span (20 mm), w is the specimen width (mm) and t is the specimen thickness (mm). Fractography analysis of the broken bar specimen was performed to investigate the fracture behaviors using SEM or FE-SEM to track the possible starting point during fracture. The elastic

Please cite this article in press as: Kim J-H, et al. Mechanophysical and biological properties of a 3D-printed titanium alloy for dental applications. Dent Mater (2020), https://doi.org/10.1016/j.dental.2020.04.027

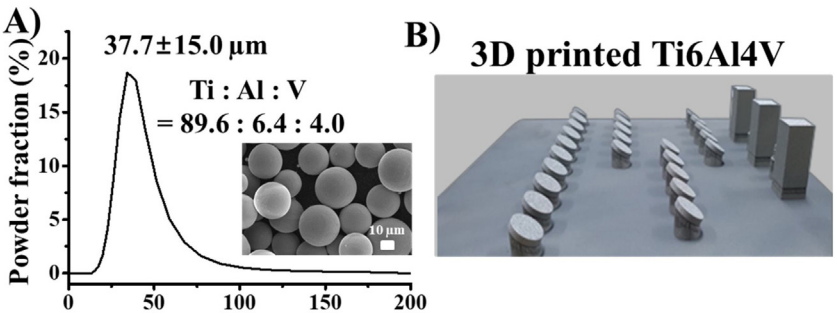

Fig. 1 – Ti-6Al-4V powder characterization for use in the 3D-printed dental materials. (A) Ti-6Al-4V particle size (37.7 ± 15.0 μm) distribution by the powder analyser, spherical morphology by SEM and their composition (89.6% Ti, 6.4% Al and 4.0% V (wt%)) by EDS. (B) Fabrication of various structures (specimens) using a direct laser metal sintering 3D printer. Several specimen of disk (d = 10 mm and h = 2 mm) and cuboid shape (10.0 × 10.0 × 20.0 mm) were 3D-printed.

modulus of the lattice structure (10.0 × 10.0 × 20.0 mm) was measured by compressive strength analysis using Bluehill software (version 3.31, Instron) according to the span width (0.3, 0.5, 1.0 mm or dense block type).

2.4. *Surface characteristics of the specimens for the in vitro study*

The surface of the disk specimens for the in vitro study was observed using SEM for the different surface treatments (as 3D-printed, 3D + sand-blasted, 3D + polished). The surface roughness was measured using a surface roughness analyser (SJ-400, Mitutoyo, Kawasaki, and Japan) to measure Ra (arithmetical mean), Ry (maximum height), and Rz (height irregularities, n = 5). Scan was conducted at a speed of 5 mm/s with measurement width (4 mm) and cut-off values (0.8 mm). The average value of three measurements is reported as the representative value for each specimen. The hydrophilicity of the specimen surfaces was measured by contact angle analysis using a Surface Electro Optics instrument (PHX300, SEO, Suwon, Korea) and distilled water (10 μL and n = 5).

2.5. *Cell culture*

hMSCs (PCS-500-012, ATCC, Manassas, VA, USA) were cultured in a bone marrow-mesenchymal stem cell growth medium (ATCC) that was supplemented with 7% fetal bovine serum (FBS, Gibco, Grand Island, NY, USA), 15 ng/ml recombinant human insulin-like growth factor (rh IGF-1), 125 pg/ml recombinant human fibroblast growth factor (rh FGF-b), 2.4 mM L-alanyl-L-glutamine and 1% penicillin/streptomycin (Gibco) according to the recommendations provided by the manufacturer. Human dermal fibroblasts (hDF, PH10605AK, Genlantis, San Diego. CA, USA) were cultured with high glucose Dulbecco's modified Eagle's medium (DMEM) supplemented with 10% FBS and 1% penicillin/streptomycin. The cells were cultured in a humidified atmosphere of 5% CO^2 at 37 °C [24,25].

2.6. *Initial cell adhesion test*

To investigate the initial cell adhesion ability on different Ti-6Al-4V specimens (machine-cut, as-given specimen after CNC cutting without 3D printing technology, or 3D + sand-blasted specimen), 200 μL of the hMSC or hDF cell (2×10^4) suspensions was placed on top of the specimen with the above specific growth media. 3D + sand-blasted specimen was chosen after consideration of hydrophilicity and 3D printing needs for maintaining complex architectures, which cannot be attained via other post-treatment conditions. Machine-cut without any surface treatment (grade5, Kobelco, Kobe, Hyogo, Japan) and 3D + sand-blasted specimen from powder (grade5, Advanced Powders & Coatings Inc. QC, Canada) are all from Ti-6Al-4V of grade5 with a 10 mm diameter and 2 mm thickness. After 4 h, 800 μL of the growth media was added, and incubated for 8 h. Then, the cells were fixed with ice-cold 4% paraformaldehyde for 30 min. The fixation solution was then removed, and all specimens were washed with phosphate-buffered saline (PBS). Then, cell membrane permeabilization was conducted for 5 min using 0.2% Triton X-100 (T8787, Sigma Aldrich, St. louis, MO, USA). After being washed with PBS 3 times, all specimens were immersed in 1% bovine serum albumin (BSA) solution (BAH68, Equitech-bio, Kerrville, TX, USA) to block nonspecific protein interactions. The blocked specimens were incubated with an anti-vinculin (1:200, mouse, sc-73614, Santa Cruz Biotechnology Inc, Dallas, TX, USA) primary antibody overnight at 4 °C with 1% BSA. All specimens were washed three times with PBS and then further incubated with rhodamine (TRITC)-conjugated donkey-anti-mouse (1:400, 715-025-150, West Grove, PA, USA) for 1 hr with 1% BSA. Then, 488 phalloidin (1:400, A12379, Thermo Fisher Scientific, Waltham, MA, USA) and 4′,6-diamidino-2-phenylindole (DAPI) (1 μg/ml, 62248, Thermo Fisher Scientific) stains were applied. After the specimens were transferred to a microscope cover glass, vinculin focal adhesion (red), actin (green), and DAPI (blue) were captured with an inverted microscope (Olympus, IX71, Tokyo, Japan) with a 20x objective (Fluor 0.45). In particular, vinculin was observed from five different samples to quantify the fluorescence intensity (n = 5, ImageJ version v1.52a).

2.7. *Stem cell differentiation*

The hMSCs (2×10^4) seeded on the disk specimens (machine-cut, as-given specimen after CNC cutting without 3D printing technology, or 3D + sand-blasted specimens) or 24-well tissue culture plates (TCPs) for 24 h were differentiated

Please cite this article in press as: Kim J-H, et al. Mechanophysical and biological properties of a 3D-printed titanium alloy for dental applications. Dent Mater (2020), https://doi.org/10.1016/j.dental.2020.04.027

with osteogenic media supplemented with ascorbic acid (50 μg/mL), b-glycerophosphate (10 mM), and dexamethasone (100 nM) with a media change every 2–3 days until 14 or 21 days were reached. To investigate the osteogenic capacity of the 3D-printed specimens, real-time polymerase chain reaction (PCR) and Alizarin red S (ARS) staining were performed according to the methodology in the literature [26,27]. Briefly, at day 14, 1 μg of extracted ribonucleic acid (RNA) was transcribed to complementary deoxyribonucleic acid (cDNA), and quantitative PCR experiments were performed using a real-time PCR machine (StepOne-Plus, Applied Biosystems). The gene expression of osteocalcin (OCN) and osteopontin (OPN) were normalized to that of B-actin. The growth media culture on TCP for 14 days was used as a negative control. The primer sequences used for the real-time PCR analysis were as follows: B-actin, forward 5′-CATGGATGATGATATCGCCGCG-3′ reverse 5′-ACATGATCTGGGTCATCTTCTCG-3′; OCN, forward 5′-GTGCAGCCTTTGTGTCCAAGCAGGA-3′ reverse 5′-CCGTAGAAGCGCCGATAGGCC-3′; and OPN, forward 5′-CCCATCTCAGAAGCAGAATCTC-3′ reverse 5′-ATGGCTTTCGTTGGACTTACT-3′. On day 21, the cells were stained with a 2% ARS solution (pH 4.2) for 30 min [28], and images were captured by optical microscopy (Olympus lX71, Shinjuku, Tokyo, Japan). All experiments were independently performed in triplicate, and the representative data set and images are shown.

3. Results

3.1. *Powder characterization and preparation of specimens using a 3D printer*

The Ti-6Al-4V powder size (powder analyser), morphology (FE-SEM) and composition (EDS) were initially investigated (Fig. 1A). The mean powder size and standard deviation were 37.7 ± 15.0 μm. The FE-SEM images revealed spherical particles with a size that was in agreement with the results of the mean powder size. The EDS analysis displayed a typical composition of Ti-6Al-4V with 89.6% Ti, 6.4% Al and 4.0% V (wt%). Various shapes of 3D-printed specimens were successfully produced (Fig. 1B).

3.2. *Surface pores and total pore area*

Cross-sectioned disk specimens were observed using SEM from three different areas (Fig. 2A). Regardless of the laser spacing, pores were detected in all cross-sectional areas. In particular, the number of pores that were visualized increased as the laser spacing increased. The mean surface pores and total pore area showed significant increases with increasing laser spacing ($P < 0.05$, Fig. 2B). A narrow laser spacing (30–50 μm) showed a relatively low number of pores (45–63 each per specimen) than the pores (104–232 each per specimen) from a large laser spacing (60–100 μm). The total pore area was smaller (3.6–5.9 mm^2 per cross-sectioned single plane) for small laser spacings (30–60 μm) than for large laser spacings (70–100 μm, 9.8–11.5 mm^2 per cross-sectioned single plane). The specimen with a 80 μm laser spacing was observed at a high magnification, and unsintered powder beads were detected inside the specimen (Fig. 2C).

3.3. *Mechanical properties and fractography*

The three-point flexural strength and elastic modulus were investigated as a function of the laser spacing (30, 50, 70 and 90 μm) using a bar specimen. The mean values and standard deviation of the three-point flexural strength and elastic modulus are shown with the representative stress-strain curves (Fig. 3A and B). The representative stress-strain curves displayed the lowest flexural stress and lowest strain (~0.7) for the 90 μm laser spacing. The three-point flexural strength of each group (1000–2000 MPa) descended according to an increase in the laser spacing (30 > 50 > 70 > 90 μm, $P < 0.05$). The elastic modulus (52~78 GPa) also descended according to an increase in the laser spacing (30, 50 > 70 > 90 μm, $P < 0.05$). Fractography was performed on the fractured surface of the bar specimen. The number of unsintered beads detected during SEM analysis increased as the laser spacing increased (Fig. 3C). In particular, the initial fracture of the bar specimen was observed for the specimens with laser spacings of 70 or 90 μm, and they displayed pores and defects at the possible crack initiation points (red arrow, Fig. 3D).

Representative stress-strain curves from the 3D-printed lattice architectures and their elastic moduli are shown in Fig. 4. The lattice specimen with a 0.3 mm diameter span displayed ductile behavior (~20 times lower elastic modulus with larger strain) compared to the block specimen. Overall, as the span diameter increased, the elastic modulus increased (0.3 < 0.5 < 1.0 mm < block, $P < 0.05$).

3.4. *Surface characteristics for the in vitro study*

The as-3D-printed specimens and other surface-modified specimens (3D + sand-blasted and 3D + polished) were compared in terms of their surface characteristics. The as-3D-printed specimen contained round and irregular spherical particles (unsintered powder) on the surface in the SEM image. After surface treatment (3D + sand-blasted and 3D + polished), the unsintered spherical particles were removed (Fig. 5A). When the surface roughness (Ra) was measured, the as-3D-printed specimen (8.3 ± 0.2 μm) had a value that was 3~14 times higher than that of the others (3D + sand-blasted (2.3 ± 0.3 μm) and 3D + polished (0.6 ± 0.1 μm), $P < 0.05$, Fig. 5), while the 3D + polished sample had the lowest value among the groups measured. Other roughness aspects (Ry and Rz) were shown as having similar trends among groups. The contact angle was measured using deionized water (DW) to investigate the surface hydrophilicity (Fig. 5C). The contact angle significantly decreased for the as-3D-printed specimen (114.9 ± 1.9°) after sand blasting (68.7 ± 2.6°) or rough polishing (54.5 ± 2.1°, $P < 0.05$). Due to the presence of unsintered particles and the resulting high water contact angle value, the as-3D-printed condition was excluded for further in vitro study. In addition, 3D + polished condition could not meet the 3D printing needs for complicated architectures in the dental field; thus, only the 3D + sand-blasted condition was chosen for further in vitro study.

Please cite this article in press as: Kim J-H, et al. Mechanophysical and biological properties of a 3D-printed titanium alloy for dental applications. Dent Mater (2020), https://doi.org/10.1016/j.dental.2020.04.027

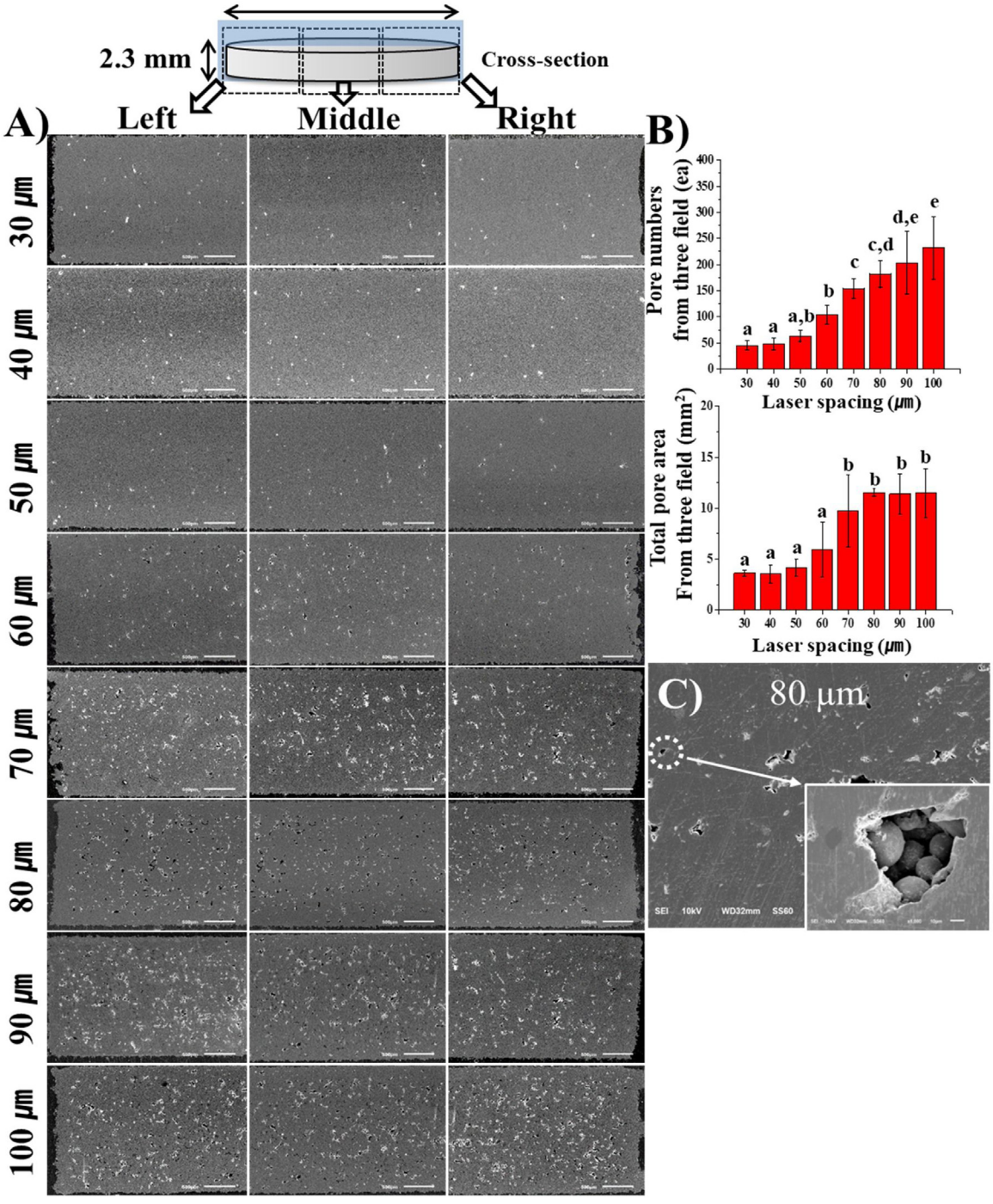

Fig. 2 – The surface pores and total pore area of the cross-sectioned 3D-printed disk specimens as a function of the laser spacing during 3D printing (30–100 μm). (A) Cross-sectioned SEM images revealing pores (scale bar = 500 μm). (B) Pore numbers decreased as the laser spacing decreased (30–50 μm) than large laser spacing counterparts (60–100 μm). The total pore area was smaller for a narrow laser spacing (30–60 μm) than for a large laser spacing (70–100 μm). Different letters indicate significant differences among samples ($n = 3$, $P < 0.05$). (C) SEM image of 80 μm laser spacing. The surface pores were representatively magnified to observe the unsintered Ti-6Al-4 V beads inside the specimen (scale bar = 10 μm).

3.5. *Cell adhesion and cell differentiation*

Cell adhesion tests were conducted for 12 h using hDF and hMSC cells on two different Ti-6Al-4V specimens (machine-cut, as-given specimen after CNC cutting without 3D printing technology, and 3D + sand-blasted). The machine-cut Ti-6Al-4V specimens were used as controls for comparing biological effects with those of the 3D + sand-blasted specimens. Representative fluorescence microscopy images for actin (green), vinculin (red), and nucleus (blue) staining revealed compara-

Please cite this article in press as: Kim J-H, et al. Mechanophysical and biological properties of a 3D-printed titanium alloy for dental applications. Dent Mater (2020), https://doi.org/10.1016/j.dental.2020.04.027

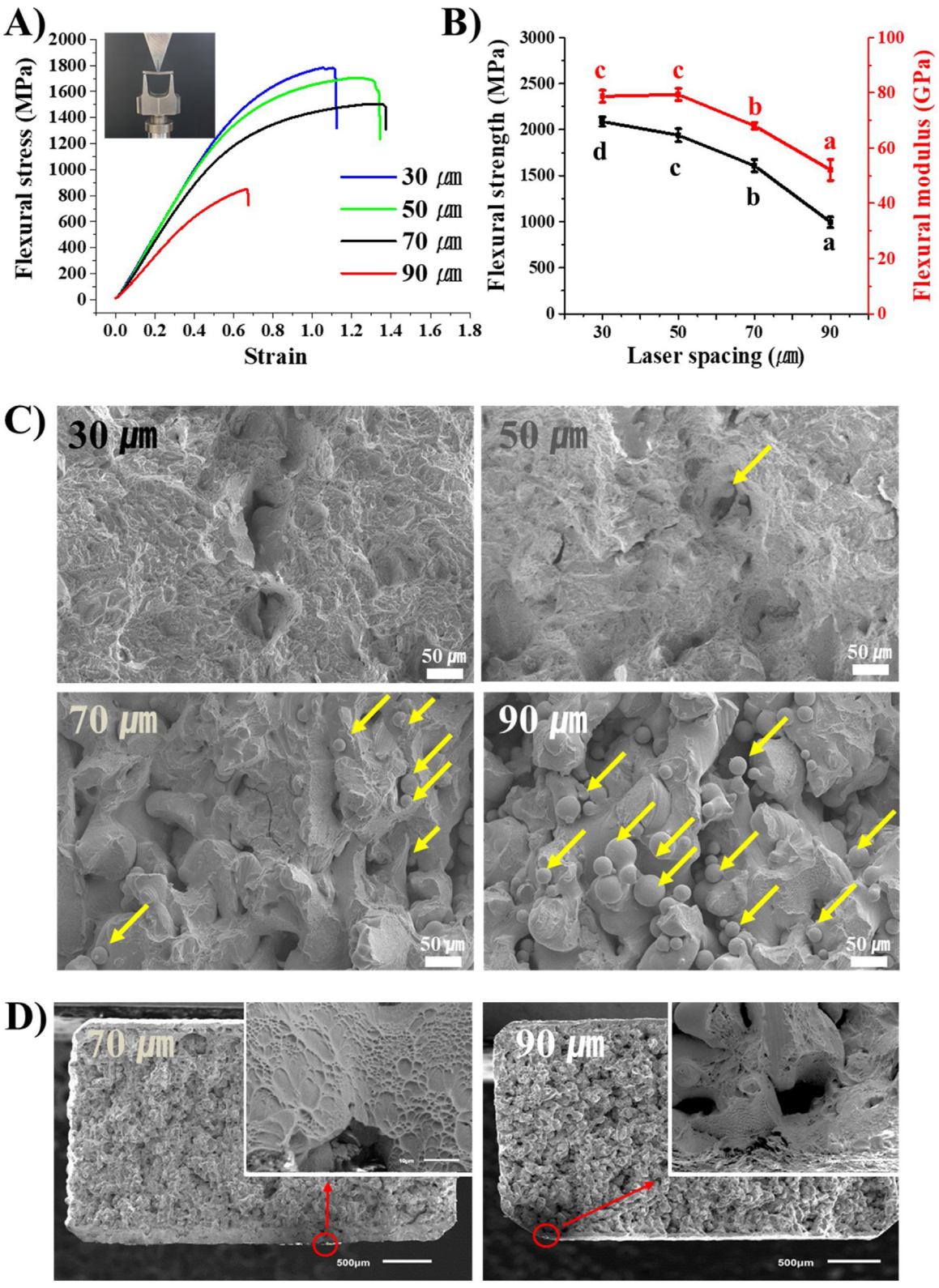

Fig. 3 – Mechanical test of 3D-printed specimens and their fractography. (A and B) The three-point flexural strength and elastic modulus are shown with the representative stress-strain curve with the testing image (insert in A). The mechanical strength and modulus decreased as the laser spacing increased. Different letters indicate significant differences among samples ($n = 5$, $P < 0.05$). (C) FE-SEM image of the fractured surface after the three-point flexural test. Yellow arrows indicate unsintered beads that were especially present in the 70 and 90 μm groups. (D) SEM image fractography of bar specimens (70 and 90 μm). Red arrows indicate pores and defects at the crack initiation point. (For interpretation of the references to color in this figure legend, the reader is referred to the web version of this article.)

Please cite this article in press as: Kim J-H, et al. Mechanophysical and biological properties of a 3D-printed titanium alloy for dental applications. Dent Mater (2020), https://doi.org/10.1016/j.dental.2020.04.027

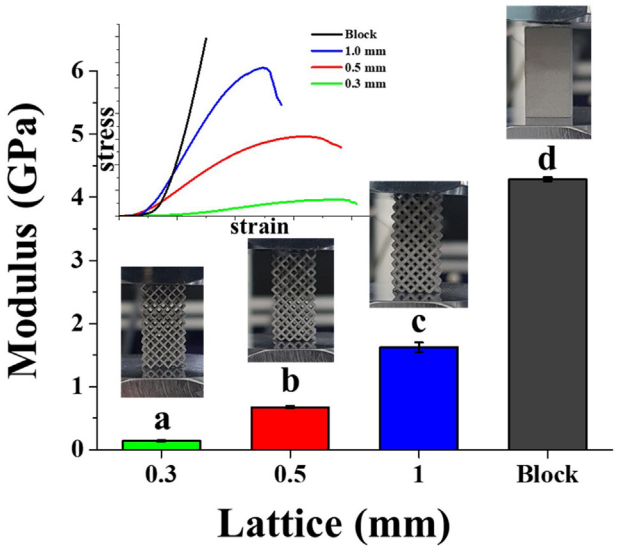

Fig. 4 – Modulation of the elastic modulus in the 3D-printed Ti-6Al-4V specimens from 50 μm laser spacing as a function of the lattice structure (0.3, 0.5, and 1 mm span width or dense block specimen). Representative stress-strain curves of the cubic lattice structure during compressive testing and the calculated elastic modulus values. Compared to the modulus of the dense block, the elastic modulus of the 0.3–1 mm lattice architectures were 3–30 times less than that of dense block, respectively, and they had more flexibility (high strain), providing the possibility of adjusting the elastic modulus to minimize stress concentrations. The different letters indicate significant differences among the samples ($n = 3$, $P < 0.05$).

ble hDF and hMSC adhesion morphologies on both surfaces (Fig. 6A and B). Neither the hDF nor the hMSC cells showed differences in cell count as a function of the surface treatment (not shown). Additionally, the expression of the cell adhesion protein (vinculin) was semi-quantified, and a comparable intensity was revealed from both the 3D + sand-blasted and machine-cut surfaces ($P > 0.05$, Fig. 6C). Next, a differentiation study was performed using hMSCs. As a result of hMSC differentiation on the substrates, the machine-cut condition revealed a similar ARS staining (red color) to the 3D + sand-blasted counterpart after 21 days of culture (Fig. 7A). Osteogenic gene expression (OPN and OCN) at day 14 from the 3D + sand-blasted and machine-cut conditions showed comparable and high fold changes compared to that of the negative control (growth media culture on TCP, Fig. 7B).

4. Discussion

The null hypotheses were partially accepted. The first null hypothesis that there are no differences in the mechanical properties due to the laser spacing (30–100 μm) was rejected because the mechanical properties measured with the three-point flexural test revealed a significant decrease in strength and modulus for the large laser spacing groups due to inner defects. On the other hand, the second null hypothesis that there are no differences in biological properties, such as cell adhesion and osteogenesis from stem cells, between the optimized 3D-printed and machine-cut specimens was accepted as a result of the in vitro results. The present investigation was designed to evaluate the biological activities between machine-cut and 3D-printed specimens after optimizing the DLMS 3D-printing conditions according to the mechanophysical characteristics. It is worth noting that the 3D-printed specimens optimized in this study had comparable biological properties from human fibroblasts and mesenchymal stem cells, which are major cell types of interest that contact oral tissues, such as facial skin and bone.

Within the last 15 years, DLMS processes were introduced as one of the 3D-printing technologies available for metal-based biomaterials, and they are commercially available to make customized dental or medical devices (i.e., dental/medical implants or dental products) due to their great reproducibility with relatively good resolution (~20 μm), the ability to make complex 3D architectures, and cost effectiveness for the fabrication of individual parts [16–18]. However, the mechanical strength was generally an issue in 3D-printed metal parts due to the presence of inner defects and unsintered powder, which led to questions about their biological activities when implanted in oral tissues [29]. In particular, 3D-printed dental materials should have good mechanical properties because they maintain their inner and outer morphology during high stress conditions, such as a normal or even an abnormal biting force (i.e., bruxism) [30,31]. Here, DLMS 3D-printing conditions were optimized using medical-grade Ti-6Al-4 V powders based on two parameters: the laser spacing (30–100 μm) and post-surface treatment (as-given or sand blasted). The inner defect pore amount, mechanical properties, roughness and hydrophilicity were evaluated under different conditions.

After briefly assessing the characteristics of medical-grade Ti-6Al-4V powders in terms of size (37.7 ± 15.0 μm), spherical morphology, and element composition as Ti-6Al-4 V powders without foreign elements (Ti:Al:V = 89.6:6.4:4.0), the DLMS 3D printing ability in different architectures (disk, cubic, and lattice) was initially checked (Fig. 1). Next, the laser spacing and

Please cite this article in press as: Kim J-H, et al. Mechanophysical and biological properties of a 3D-printed titanium alloy for dental applications. Dent Mater (2020), https://doi.org/10.1016/j.dental.2020.04.027

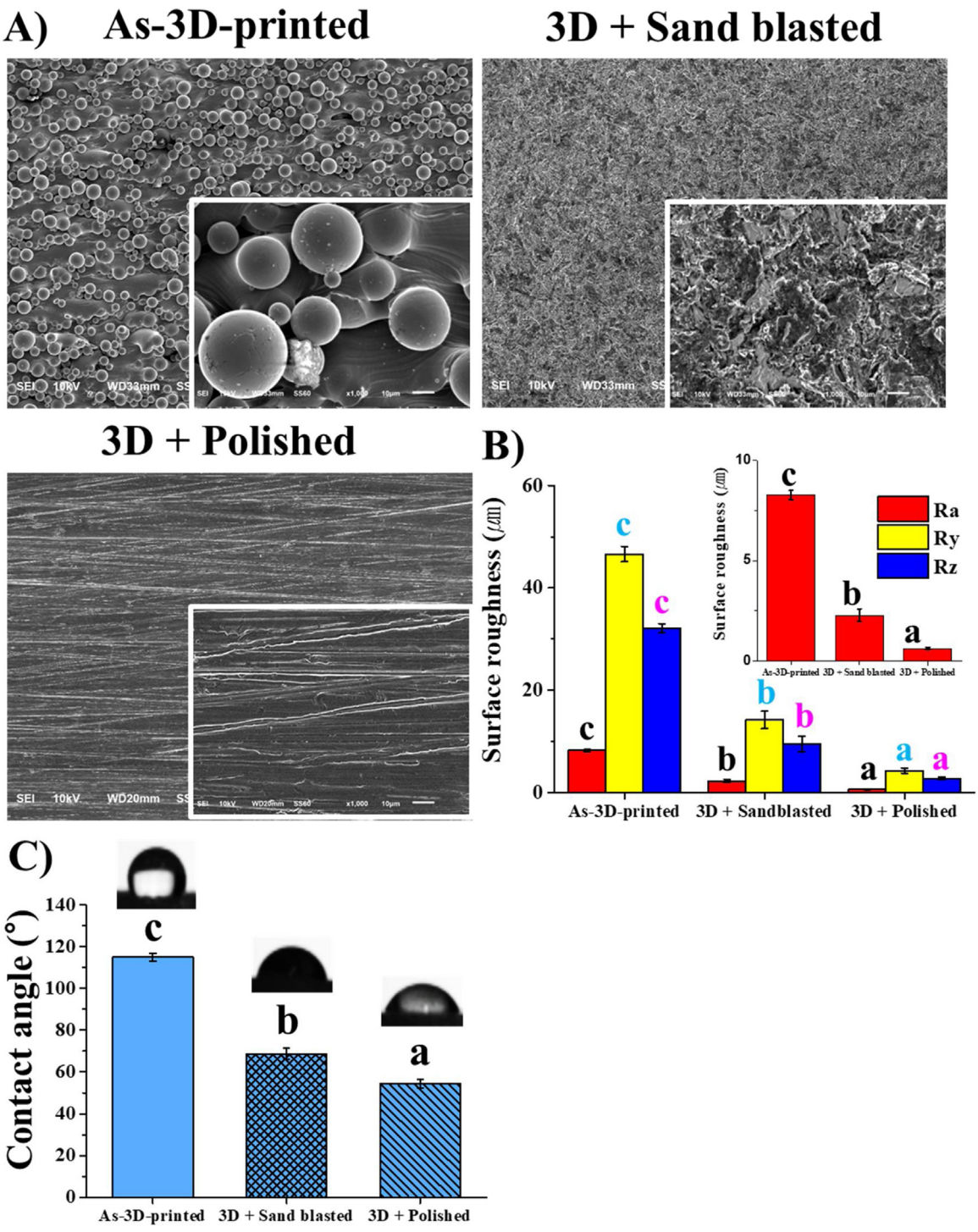

Fig. 5 – Optimization of the post-surface treatment using the sand blasting process after 3D printing to produce physicochemical properties which are beneficial than those from as-3D printed specimens. (A) SEM analysis revealed that the as 3D-printed specimen had irregularly sized and spherical particles on the surface, while the sand-blasted specimen (3D + sand-blasted) displayed a complete absence of powders on the surface along with those of 3D + polished group. (B and C) Surface roughnesses (Ra, Ry and Rz) and water contact angle (hydrophilicity) values. The as-3D-printed specimen revealed a 3–14 times higher Ra value than that of the others ($P < 0.05$), which is considered an inappropriate surface topography for cell adhesion. The contact angle significantly decreased for the as-3D-printed specimen (114.9 ± 1.9°) after sand blasting (68.7 ± 2.6°, $P < 0.05$), which are values that are relatively similar to those for the rough-polished group (54.5 ± 2.1°, $P < 0.05$) as compared to those of as-3D-printed specimen (114.9 ± 1.9°); this would be considered a cytocompatible hydrophilic material. Different letters indicate significant differences in the surface roughness and contact angle values among the samples ($n = 5$, $P < 0.05$).

Please cite this article in press as: Kim J-H, et al. Mechanophysical and biological properties of a 3D-printed titanium alloy for dental applications. Dent Mater (2020), https://doi.org/10.1016/j.dental.2020.04.027

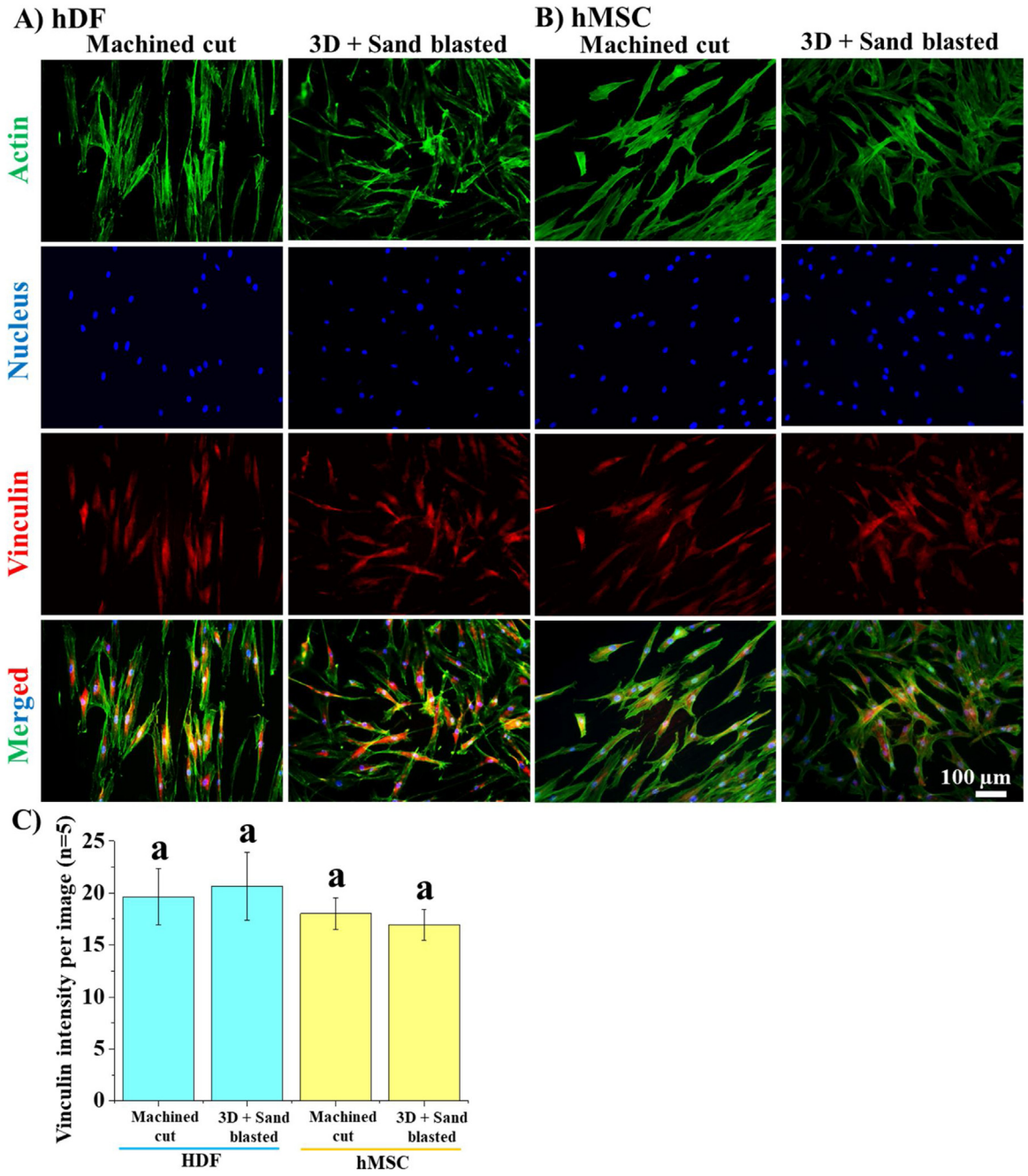

Fig. 6 – Initial cell adhesion test on optimized 3D-printed specimen (3D + sand-blasted) using hDF and hMSC for 12 h. The machine-cut specimen was used as the control group to compare the biological effects with those for the 3D + sand-blasted specimen. (A and B) Representative fluorescence microscopy images after actin (green), vinculin (red), and nucleus (blue) staining revealed comparable hDF and hMSC adhesion morphologies on both surfaces. Neither hDF nor hMSC cells showed differences in the cell count depending on surface treatment (not shown). (C) Expression of cell adhesion protein (vinculin) was semi-quantified and revealed a comparable expression for both the 3D + sand-blasted and machine-cut surfaces ($n = 5$, $P > 0.05$). (For interpretation of the references to color in this figure legend, the reader is referred to the web version of this article.)

laser gap for sintering the Ti-6Al-4V powder during the 3D printing process was varied to make disk specimens after considering the powder diameter ($37.7 \pm 15.0\,\mu m$) from 30 to $100\,\mu m$ (Fig. 2). According to the results of the pore (defect) number and total pore area measurements in the cross-section specimens, the number of pores and the total pore area increased as the laser spacing increased ($30 < 70 \leq 100\,\mu m$), which could decrease the mechanical properties. The 3D-printed specimen with a narrow laser spacing had fewer pores and a smaller pore area, consistent with the previous literature

Please cite this article in press as: Kim J-H, et al. Mechanophysical and biological properties of a 3D-printed titanium alloy for dental applications. Dent Mater (2020), https://doi.org/10.1016/j.dental.2020.04.027

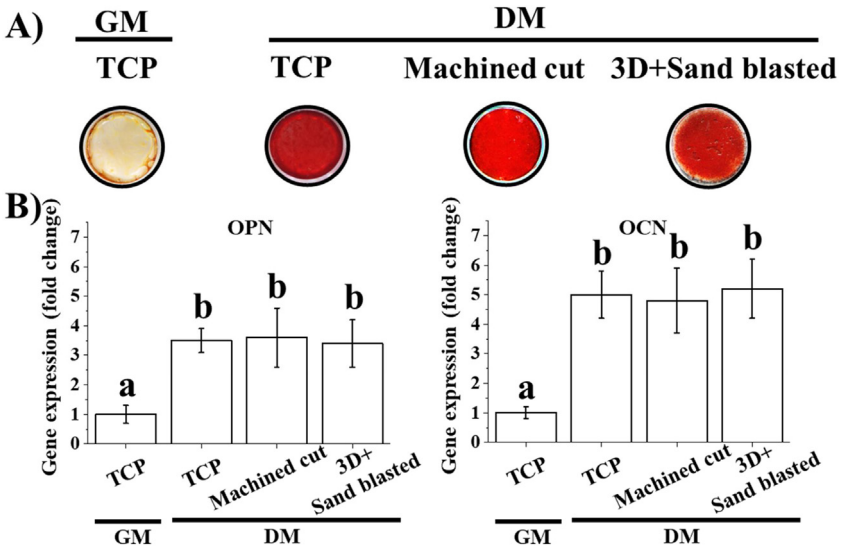

Fig. 7 – Comparable hMSC differentiation ability for the 3D-printed Ti-6Al-4V substrates and their machine-cut counterpart. (A) Machine cut conditions revealed similar ARS staining (red color) to the 3D + sand-blasted after 21 days of culture under osteogenic differentiation media (DM). (B) Osteogenic gene expression (OPN and OCN) at day 14 for the 3D + sand-blasted and machine cut conditions showed comparable and high fold changes compared to that of the negative control (growth media (GM) culture on tissue culture plate (TCP), $n = 3$, $P < 0.05$). (For interpretation of the references to color in this figure legend, the reader is referred to the web version of this article.)

[32–34]. Pores, micro cracks and specimen flaws caused stress concentrations, induced cracks and decreased the mechanical properties [35]. In particular, the number of pores and the total pore area were the main factors that influenced the mechanical strength [36,37]. An increase in the laser spacing accelerated the 3D printing speed and decreased the production time, but achieving the desired mechanical properties is more important for the application of 3D-printed specimens to dental fields that require a high mechanical strength. To confirm the difference in the mechanical properties depending on the laser spacing (30, 50, 70, and 90 μm as representatives), a three-point flexural strength test was performed and revealed that the highest flexural strength and modulus herein were detected in the 30 or 50 μm groups, while the lowest value was detected in the 90 μm group (Fig. 3A and B). 800–1800 MPa was detected in 3D-printed specimens, revealing

Based on these results, samples' strength values from 30 to 70 μm groups (1500–1800 MPa) were in a range of mechanical properties (850–1900 MPa) reported elsewhere from CNC-cut or sintered Titanium or Ti6Al4V which are used in the biomedical field [38–41]. Within the limitation of different testing conditions of specimens such as fabrication techniques (CNC cutting or sintering), sample size, and cross-head speed, 3D-printed specimens were considered to have appropriate mechanical properties for biomedical applications, possibly resisting biting force in the orofacial system. The standard for medical graded titanium alloy (ASTM B348-02) mentioned a requirement of values of 895 MPa for tensile strength, which is necessary to be considered for clinical usage of 3D-printed specimens [42].

When the fractured surface after the three-point flexural strength test was examined by FE-SEM, unsintered spherical beads (yellow arrow) were less frequently detected in the 30 and 50 μm groups than in the other groups (Fig. 3C). According to fractography analysis, defects on the bottom side of the specimen seemed to propagate along the fracture line (Fig. 3D). Thus, a 50 μm laser spacing was chosen to fabricate a complex lattice architecture based on mechanical properties that were similar to those for a 30 μm laser spacing. One of the merits of utilizing 3D printing is the ability to fabricate customized shapes with different bulk elastic moduli and various architectures to match those of the surrounding tissues, especially bone, to minimize stress concentrations [43]. To check this possibility, 0.3–1 mm lattice and dense cubic structures were 3D printed with the same external appearance, and the compressive elastic modulus was evaluated (Fig. 4). Compared to the modulus of the dense block, the 0.3–1 mm lattice architectures had a modulus that was 3–30 times lower and with more flexibility (higher strain), which provides the possibility of adjusting the elastic modulus to minimize the stress concentration in natural bone tissues. Therefore, dentists and dental technicians should consider the versatility of the mechanical properties of 3D-printed specimens that depend on the design of the final structure.

To assess the biological properties of the 3D-printed Ti-6Al-4V specimen, the surface morphology, roughness and hydrophilicity after surface treatment were determined, as shown in Fig. 5. The as-given specimen surface had irregular and round particles of the Ti-6Al-4V powder and had a very large surface roughness (Ra = ~8 μm) and high contact angle (~110°). These spherical particles are known to hinder bone differentiation [32,44]. Therefore, further surface treatment is necessary after 3D printing to enable good initial cell adhesion. The surface can be conventionally post-treated by polishing, chemically treating (with NaOH, HF or HCl), or sand blasting to produce a clean surface. Three-dimensional

Please cite this article in press as: Kim J-H, et al. Mechanophysical and biological properties of a 3D-printed titanium alloy for dental applications. Dent Mater (2020), https://doi.org/10.1016/j.dental.2020.04.027

architectures are difficult to polish, and chemical treatments change the surface chemistry, which can affect cell behavior [33,45,46]. Thus, a sand blasting post-treatment was chosen for removing the unsintered powder from the surface of the 3D-printed specimens. The sand-blasting conditions for the 3D-printed specimens were optimized based on the sand-blaster pressure (4.3 bar) and powder (50 μm alumina) for a certain time to physically remove unsintered powder from the outer surface while minimizing any change in the overall morphology (data not shown). A surface free of unsintered powder particles was produced with a slight roughness (~2.5 μm) and relatively hydrophilic surface (~70°); these properties from sand-blasting treatment are more beneficial compared to as-produced 3D-printed specimens along with the positive control group that consisted of a 3D-printed surface polished with SiC #220 paper. The surface roughness and hydrophilicity are key factors for cell adhesion and cell differentiation. A high Ra in the range from 2 to 5 μm is known to increase the surface area of the implant and improve the adhesion of cells, but a very high Ra of 5 μm had a detrimental effect on the cell differentiation [47–49]. In addition, the 3D + polished condition, causing destruction of 3D-printed architectures during the polishing process, could not meet the 3D printing needs for complicated architectures in the dental field; thus, only the sand-blasted 3D-printed specimens (3D + sand-blasted) were used for further biological tests. Optimization of surface texture after 3D-printing and sand-blasting is necessary for further increasing biological effects of target cells because surface topology including direction of surface groove or nanostructure physically affect direction of (stem) cell response [3,50–53].

Next, the initial hDF and hMSC adhesion tests for 12 h were performed on the sand-blasted 3D-printed specimens (3D + sand-blasted) (Fig. 6). The hDF and hMSC values are representative for the direct-contact cell types of orofacial mucosa and bone, respectively. A machine-cut Ti-6Al-4V specimen from a CNC machine without additional surface modification was used as the control group, which is a widely used minimum control group and was compared with an optimally adjusted 3D-printed specimen (3D + sand-blasted). Representative fluorescence microscopy images revealed similar nucleus (blue) numbers and adhesive protein levels, which were expressed by vinculin (red) in both groups. Aligned and randomly oriented actin filaments were observed for the machine-cut and 3D + sand-blasted conditions, respectively, due to their innately different surface textures. Finally, hMSC differentiation on the specimens was conducted for up to 21 days under osteogenic media to measure the osteogenic gene expression as well as biomineralization. The 3D-printed Ti-6Al-4V substrates (3D + sand-blasted) displayed a similar biomineralization ability by ARS staining (red color) and osteogenic gene expression (OCN and OPN) by qPCR assay to that of the machine-cut Ti-6Al-4V substrate along with the osteogenesis of 3D-printed titanium or titanium alloys from other literature reports [20,54,55]. In summary, optimally DLMS 3D-printed Ti-6Al-4V specimens had similar biological properties to their machine-cut counterparts, suggesting the potential usefulness of 3D printing technology for multiple dental applications.

The limitations of this study include the need for further optimization of the 3D printing conditions to produce zero defects from the different laser wavelengths and powers as well as powder sizes and shapes. Further in vivo and clinical tests are required to investigate the mechanical and biological properties of 3D-printed specimens in dental applications.

5. Conclusion

Within the limitations of this investigation in mind, it was shown herein that the laser spacing during DLMS 3D printing affected the number of pores, total pore area and mechanical properties. An optimized post-surface treatment by sand blasting improved the water hydrophilicity due to a decrease in the surface roughness to an appropriate range. The optimized DLMS 3D-printed Ti-6Al-4V specimens had comparable biological properties to their machine-cut counterparts, suggesting the potential usefulness of 3D printing technology for multiple dental applications, including customized dental implants and other implantable prosthodontics.

Acknowledgements

This work was supported by a National Research Foundation of Korea (NRF) grant funded by the Ministry of Science and ICT (2017R1C1B5076179, 2019R1C1C1002490 and 2020R1A2C1005867), by the Global Research Development Center Program (2018K1A4A3A01064257) and Priority Research Center Program by the Ministry of Education (2019R1A6A1A11034536). The present research was also supported by the research fund of Dankook university in 2019 for the University Innovation Support Program and Sentrol Co., Ltd. (Seoul, Korea).

REFERENCES

[1] Park I-S, Mahapatra C, Park JS, Dashnyam K, Kim J-W, Ahn JC, et al. Revascularization and limb salvage following critical limb ischemia by nanoceria-induced Ref-1/APE1-dependent angiogenesis. Biomaterials 2020:119919.
[2] Jun S-K, Yoon J-Y, Mahapatra C, Park JH, Kim H-W, Kim H-R, et al. Ceria-incorporated MTA for accelerating odontoblastic differentiation via ROS downregulation. Dental Mater 2019;35:1291–9.
[3] Lee J-H, Kim D-H, Lee H-H, Kim H-W. Role of nuclear mechanosensitivity in determining cellular responses to forces and biomaterials. Biomaterials 2019;197:60–71.
[4] De Caluwé T, Vercruysse CWJ, Ladik I, Convents R, Declercq H, Martens LC, et al. Addition of bioactive glass to glass ionomer cements: effect on the physico-chemical properties and biocompatibility. Dental Mater 2017;33:e186–203.
[5] Blache U, Stevens MM, Gentleman E. Harnessing the secreted extracellular matrix to engineer tissues. Nat Biomed Eng 2020.
[6] Hatamleh MM, Wu X, Alnazzawi A, Watson J, Watts D. Surface characteristics and biocompatibility of cranioplasty titanium implants following different surface treatments. Dental Mater 2018;34:676–83.
[7] Chai YC, Kerckhofs G, Roberts SJ, Van Bael S, Schepers E, Vleugels J, et al. Ectopic bone formation by 3D porous

calcium phosphate-Ti6Al4V hybrids produced by perfusion electrodeposition. Biomaterials 2012;33:4044–58.
[8] Cordeiro JM, Beline T, Ribeiro ALR, Rangel EC, da Cruz NC, Landers R, et al. Development of binary and ternary titanium alloys for dental implants. Dental Mater 2017;33:1244–57.
[9] Yi H-G, Choi Y-J, Jung JW, Jang J, Song T-H, Chae S, et al. Three-dimensional printing of a patient-specific engineered nasal cartilage for augmentative rhinoplasty. J Tissue Eng 2019;10, 2041731418824797.
[10] Han J, Kim DS, Jang H, Kim H-R, Kang H-W. Bioprinting of three-dimensional dentin–pulp complex with local differentiation of human dental pulp stem cells. J Tissue Eng 2019;10, 2041731419845849.
[11] Aldaadaa A, Owji N, Knowles J. Three-dimensional printing in maxillofacial surgery: hype versus reality. J Tissue Eng 2018;9, 2041731418770909.
[12] Ioannidis A, Bomze D, Hämmerle CHF, Hüsler J, Birrer O, Mühlemann S. Load-bearing capacity of CAD/CAM 3D-printed zirconia, CAD/CAM milled zirconia, and heat-pressed lithium disilicate ultra-thin occlusal veneers on molars. Dental Mater 2020.
[13] Thattaruparambil Raveendran N, Vaquette C, Meinert C, Samuel Ipe D, Ivanovski S. Optimization of 3D bioprinting of periodontal ligament cells. Dental Mater 2019;35: 1683–94.
[14] Kessler A, Reymus M, Hickel R, Kunzelmann K-H. Three-body wear of 3D printed temporary materials. Dental Mater 2019;35:1805–12.
[15] Liu F, Liu Y, Li X, Wang X, Li D, Chung S, et al. Osteogenesis of 3D printed macro-pore size biphasic calcium phosphate scaffold in rabbit calvaria. J Biomater Appl 2019;33:1168–77.
[16] Fukuda A, Takemoto M, Saito T, Fujibayashi S, Neo M, Pattanayak DK, et al. Osteoinduction of porous Ti implants with a channel structure fabricated by selective laser melting. Acta Biomater 2011;7:2327–36.
[17] Han C, Li Y, Wang Q, Wen S, Wei Q, Yan C, et al. Continuous functionally graded porous titanium scaffolds manufactured by selective laser melting for bone implants. J Mech Behav Biomed Mater 2018;80:119–27.
[18] Hollander DA, von Walter M, Wirtz T, Sellei R, Schmidt-Rohlfing B, Paar O, et al. Structural, mechanical and in vitro characterization of individually structured Ti–6Al–4V produced by direct laser forming. Biomaterials 2006;27:955–63.
[19] Cheng A, Humayun A, Cohen DJ, Boyan BD, Schwartz Z. Additively manufactured 3D porous Ti-6Al-4V constructs mimic trabecular bone structure and regulate osteoblast proliferation, differentiation and local factor production in a porosity and surface roughness dependent manner. Biofabrication 2014;6:045007.
[20] Shaoki A, Xu J-y, Sun H, Chen X-s, Ouyang J, Zhuang X-m, et al. Osseointegration of three-dimensional designed titanium implants manufactured by selective laser melting. Biofabrication 2016;8:045014.
[21] Liu H, Li W, Liu C, Tan J, Wang H, Hai B, et al. Incorporating simvastatin/poloxamer 407 hydrogel into 3D-printed porous Ti6Al4V scaffolds for the promotion of angiogenesis, osseointegration and bone ingrowth. Biofabrication 2016;8:045012.
[22] Heinl P, Müller L, Körner C, Singer RF, Müller FA. Cellular Ti–6Al–4V structures with interconnected macro porosity for bone implants fabricated by selective electron beam melting. Acta Biomater 2008;4:1536–44.
[23] Kim J-H, Im Y-W, Oh S, Kim H-W, Lee J-H, Lee H-H. Characterization of an anti-foaming and fast-setting gypsum for dental stone. Dental Mater 2019;35:1728–39.
[24] Moon H-J, Lee J-H, Kim J-H, Knowles JC, Cho Y-B, Shin D-H, et al. Reformulated mineral trioxide aggregate components and the assessments for use as future dental regenerative cements. J Tissue Eng 2018;9, 2041731418807396.
[25] Lee S-M, Kim S-Y, Kim J-H, Jun S-K, Kim H-W, Lee J-H, et al. Depth-dependent cellular response from dental bulk-fill resins in human dental pulp stem cells. Stem Cells Int 2019:1–11.
[26] Jun S-K, Yoon J-Y, Mahapatra C, Park JH, Kim H-W, Kim H-R, et al. Ceria-incorporated MTA for accelerating odontoblastic differentiation via ROS downregulation. Dent Mater 2019;35:1291–9.
[27] Dashnyam K, Buitrago JO, Bold T, Mandakhbayar N, Perez RA, Knowles JC, et al. Angiogenesis-promoted bone repair with silicate-shelled hydrogel fiber scaffolds. Biomater Sci 2019;7:5221–31.
[28] Kim D-A, Lee J-H, Jun S-K, Kim H-W, Eltohamy M, Lee H-H. Sol–gel-derived bioactive glass nanoparticle-incorporated glass ionomer cement with or without chitosan for enhanced mechanical and biomineralization properties. Dental Mater 2017;33:805–17.
[29] Chae MP, Rozen WM, McMenamin PG, Findlay MW, Spychal RT, Hunter-Smith DJ. Emerging applications of bedside 3D printing in plastic surgery. Front Surg 2015;2:25.
[30] Daou EE. The zirconia ceramic: strengths and weaknesses. Open Dent J 2014;8:33–42.
[31] Spies BC, Nold J, Vach K, Kohal RJ. Two-piece zirconia oral implants withstand masticatory loads: an investigation in the artificial mouth. J Mech Behav Biomed Mater 2016;53:1–10.
[32] Traini T, Mangano C, Sammons RL, Mangano F, Macchi A, Piattelli A. Direct laser metal sintering as a new approach to fabrication of an isoelastic functionally graded material for manufacture of porous titanium dental implants. Dental Mater 2008;24:1525–33.
[33] Heinl P, Muller L, Korner C, Singer RF, Muller FA. Cellular Ti-6Al-4V structures with interconnected macro porosity for bone implants fabricated by selective electron beam melting. Acta Biomater 2008;4:1536–44.
[34] Cansizoglu O, Harrysson O, Cormier D, West H, Mahale T. Properties of Ti–6Al–4V non-stochastic lattice structures fabricated via electron beam melting. Mater Sci Eng A 2008;492:468–74.
[35] Wang F, Williams S, Colegrove P, Antonysamy AA. Microstructure and mechanical properties of wire and arc additive manufactured Ti-6Al-4V. Metall Mater Trans A 2012;44:968–77.
[36] Chindaprasirt P, Jaturapitakkul C, Sinsiri T. Effect of fly ash fineness on compressive strength and pore size of blended cement paste. Cement Concr Compos 2005;27:425–8.
[37] Sallica-Leva E, Jardini AL, Fogagnolo JB. Microstructure and mechanical behavior of porous Ti–6Al–4V parts obtained by selective laser melting. J Mech Behav Biomed Mater 2013;26:98–108.
[38] Sarre B, Flouriot S, Geandier G, Panicaud B, Rancourt Vd. Mechanical behavior and fracture mechanisms of titanium alloy welded joints made by pulsed laser beam welding. Proc Struct Integr 2016;2:3569–76.
[39] Hsu H-C, Wu S-C, Hsu S-K, Chen C-Y, Ho W-F. Structure and mechanical properties of as-cast Ti–5Sn–xCr alloys. Mater Sci Eng A 2014;606:157–64.
[40] Amig V, Reig L, Busquets-Mataix D, Ortiz JL, Calero J. Analysis of bending strings of porous titanium processed by space holder method. Powder Metall 2011;54:67–70.
[41] Atoui JA, Felipucci DNB, Pagnano VO, Orsi IA, Nobilo MAdA, Bezzon OL. Tensile and flexural strength of commercially pure titanium submitted to laser and tungsten inert gas welds. Braz Dent J 2013;24:630–4.
[42] Nor NHM, Muhamad N, Ihsan AKAM, Jamaludin KR. Sintering parameter optimization of Ti-6Al-4V metal

Please cite this article in press as: Kim J-H, et al. Mechanophysical and biological properties of a 3D-printed titanium alloy for dental applications. Dent Mater (2020), https://doi.org/10.1016/j.dental.2020.04.027

injection molding for highest strength using palm stearin binder. Proc Eng 2013;68:359–64.
[43] Munsch M. Laser additive manufacturing of customized prosthetics and implants for biomedical applications. In: Brandt M, editor. Laser additive manufacturing. Woodhead Publishing; 2017. p. 399–420 [chapter 15].
[44] Tsutsui T, Kawaguchi H, Fujino A, Sakai A, Kaji H, Nakamura T. Exposure of macrophage-like cells to titanium particles does not affect bone resorption, but inhibits bone formation. J Orthop Sci 1999;4:32–8.
[45] Shemtov-Yona K, Rittel D, Dorogoy A. Mechanical assessment of grit blasting surface treatments of dental implants. J Mech Behav Biomed Mater 2014;39:375–90.
[46] Lee J-H, Jeong W-S, Seo S-J, Kim H-W, Kim K-N, Choi E-H, et al. Non-thermal atmospheric pressure plasma functionalized dental implant for enhancement of bacterial resistance and osseointegration. Dental Mater 2017;33:257–70.
[47] Bachle M, Kohal RJ. A systematic review of the influence of different titanium surfaces on proliferation, differentiation and protein synthesis of osteoblast-like MG63 cells. Clin Oral Implants Res 2004;15:683–92.
[48] Shaoki A, Xu JY, Sun H, Chen XS, Ouyang J, Zhuang XM, et al. Osseointegration of three-dimensional designed titanium implants manufactured by selective laser melting. Biofabrication 2016;8:045014.
[49] Tsukanaka M, Fujibayashi S, Takemoto M, Matsushita T, Kokubo T, Nakamura T, et al. Bioactive treatment promotes osteoblast differentiation on titanium materials fabricated by selective laser melting technology. Dent Mater J 2016;35:118–25.
[50] Dalby MJ, Gadegaard N, Tare R, Andar A, Riehle MO, Herzyk P, et al. The control of human mesenchymal cell differentiation using nanoscale symmetry and disorder. Nat Mater 2007;6:997–1003.
[51] Dalby MJ, Gadegaard N, Oreffo ROC. Harnessing nanotopography and integrin–matrix interactions to influence stem cell fate. Nat Mater 2014;13:558–69.
[52] Le Guéhennec L, Soueidan A, Layrolle P, Amouriq Y. Surface treatments of titanium dental implants for rapid osseointegration. Dent Mater 2007;23:844–54.
[53] Singh RK, Knowles JC, Kim H-W. Advances in nanoparticle development for improved therapeutics delivery: nanoscale topographical aspect. J Tissue Eng 2019;10, 2041731419877528.
[54] Yang F, Chen C, Zhou Q, Gong Y, Li R, Li C, et al. Laser beam melting 3D printing of Ti6Al4V based porous structured dental implants: fabrication, biocompatibility analysis and photoelastic study. Sci Rep 2017;7:45360.
[55] Ma L, Wang X, Zhao N, Zhu Y, Qiu Z, Li Q, et al. Integrating 3D printing and biomimetic mineralization for personalized enhanced osteogenesis, angiogenesis, and osteointegration. ACS Appl Mater Interfaces 2018;10:42146–54.

Please cite this article in press as: Kim J-H, et al. Mechanophysical and biological properties of a 3D-printed titanium alloy for dental applications. Dent Mater (2020), https://doi.org/10.1016/j.dental.2020.04.027